Three-Dimensional and Chemical Mapping of Intracellular Signalling Nanodomains in Health and Disease with Enhanced Expansion Microscopy

Thomas M. D. Sheard[1], Miriam E. Hurley[1], John Colyer[1], Ed White[1], Ruth Norman[1], Eleftheria Pervolaraki[1], Kaarjel K. Narayanasamy[1], Yufeng Hou[2], Hannah Kirton[1], Zhaokang Yang[1], Liam Hunter[3], Jung-uk Shim[3], Alexander H. Clowsley[4], Andrew J. Smith[1], David Baddeley[5], Christian Soeller[4], Michael A. Colman[1], and Izzy Jayasinghe[1,*]

1. School of Biomedical Sciences, Faculty of Biological Sciences, University of Leeds, Leeds LS2 9JT, UK.

2. Institute of Experimental Medical Research, Oslo University Hospital Ullevål, Oslo, Norway.

3. School of Physics and Astronomy, Faculty of Mathematics and Physical Sciences, University of Leeds, Leeds, LS2 9JT, UK.

4. Living Systems Institute, University of Exeter, Devon, EX4 4QL, UK.

5. Auckland Bioengineering Institute, University of Auckland, Auckland, New Zealand.

* Correspondence to Izzy Jayasinghe via I.Jayasinghe@leeds.ac.uk

Abstract

Nanodomains are intracellular foci which transduce signals between major cellular compartments. One of the most ubiquitous signal transducers, the ryanodine receptor (RyR) calcium channel, is tightly clustered within these nanodomains. Super-resolution microscopy has previously been used to visualise RyR clusters near the cell surface. A majority of nanodomains located deeper within cells have remained unresolved due to limited imaging depths and axial resolution of these modalities. A series of enhancements made to expansion microscopy allowed individual RyRs to be resolved within planar nanodomains at the cell periphery and the curved nanodomains located deeper within the interiors of cardiomyocytes. With a resolution of ~ 15 nm, we localised both the position of RyRs and their individual phosphorylation for the residue Ser2808. With a three-dimensional imaging protocol, we observed disturbances to the RyR arrays in the nanometre scale which accompanied right-heart failure caused by pulmonary hypertension. The disease coincided with a distinct gradient of RyR hyperphosphorylation from the edge of the nanodomain towards the centre, not seen in healthy cells. This spatial profile appeared to contrast distinctly from that sustained by the cells during acute, physiological hyperphosphorylation when they were stimulated with a β-adrenergic agonist. Simulations of RyR arrays based on the experimentally-determined channel positions and phosphorylation signatures showed how the nanoscale dispersal of the RyRs during pathology diminishes its intrinsic likelihood to ignite a calcium signal. It also revealed that the natural topography of RyR phosphorylation could offset potential heterogeneity in nanodomain excitability which may arise such RyR re-organisation.

Keywords: expansion microscopy, signalling nanodomains, site-specific phosphorylation, ryanodine receptor, computational modelling of intracellular calcium

Intracellular calcium (Ca^{2+}) nanodomains are the structural units of fast intracellular second messenger signalling mechanisms in eukaryotic cell types. Muscle,[1-3] neuronal[4, 5] and secretory cell types[6] all rely on nanodomains, which allow coordinated release of Ca^{2+} from intracellular compartments to evoke cellular responses such as contraction, modulation of electrical excitability, gene transcription and secretion. Typical nanodomains can span up to the order of 10^2 nanometres and can include the principal Ca^{2+} release channels: the ryanodine receptors (RyR) and/or inositol triphosphate receptors (IP3R). These channels are often strategically co-clustered to allow concerted opening, and may be triggered both by their neighbours (via Ca^{2+} induced Ca^{2+} release; CICR) or local signal transducers such as voltage-gated L-type calcium channels (LCC) and phospholipase-c (PLC). Junctions between the plasmalemma and the sarcoplasmic reticulum (SR) in cardiac muscle cells (also called cardiomyocytes) are among the most extensively-studied nanodomain types. Mounting evidence that the molecular constituents of nanodomains may be re-organised[7] or remodelled[8, 9] in life-threatening pathologies has emphasised the need for imaging modalities which are capable of visualising their molecular components.

The earliest measurements of the three-dimensional (3D) topology of nanodomains were made using transmission and scanning electron microscopy (EM).[10, 11] These data laid the foundation for the current paradigm of signal transduction at the nanodomain (see review on muscle).[12] The large size (~2 MDa) and square shape of the RyR tetramer is distinctly identifiable with newer EM techniques, [13-15] albeit in larger nanodomains. Fluorescence modalities, including super-resolution microscopy (e.g. techniques known by acronyms STED[16] and dSTORM[17]) have been instrumental in characterising the clustering properties of RyRs.[18, 19] DNA-based point accumulation for imaging in nanoscale topography (DNA-PAINT), implemented with total internal reflection fluorescence (TIRF) microscopy, has resolved the positions of individual RyRs within these clusters located near the cell surface.[20] It has allowed molecular-counts to be made of the regulatory protein Junctophilin-2 which co-clusters with RyR.[20] These visual insights now present new opportunities to build geometrically-realistic computational models of the local spatiotemporal patterns of Ca^{2+} signalling.[21]

A few key features in contemporary super-resolution techniques limit their utility in characterising nanodomains in primary cell types. The majority of nanodomains (>80%) in cells such as cardiomyocytes are found in deeper regions of the cell interiors, as deep as 5-15 μm from the cell surface (see supplementary figure S1 for a schematic illustration). Most single-molecule imaging techniques suffer from poor localisation accuracy at these depths. An added complication is the complex curvatures of nanodomains located deeper within the cell interiors (with diameters of 100-200 nm) [9, 15], as they wrap around tubular invaginations of the plasmalemma (known as “t-tubules”; see supplementary figure S1). Techniques such as STED [8, 19] and dSTORM have previously been used to map these interior nanodomains. 3D dSTORM (with an axial resolution of ~ 65 nm) has shown the close relationship of these nanodomains with the t-tubules;[22] however, they have only resolved the overall shapes of RyR clusters[23, 24] and not the intrinsic patterns of channel organisation within these clusters. The poorer axial resolutions of these modalities have prevented the visualisation of more intricate features and geometries of these nanodomains. Quantification of RyRs and computational modelling of RyR clusters have therefore relied upon assumptions that they form continuous, crystalline arrays[8, 21-23] as seen *in vitro*. Recent DNA-PAINT and tomographic EM data from near-surface nanodomains have shown that RyR self-assembly may be amorphous, less continuous and potentially dynamic depending on the cell’s physiology.[13, 20] A modality which offers both high in-plane and axial resolution is therefore required. 3D implementations of techniques like dSTORM have been used very effectively to resolve cellular features which are much finer than these (e.g. 3D microtubule networks,[25, 26] actin rings in neuronal axons[27] and

centrioles [26, 28]). However, the anisotropic refractive index (RI; which varies around 1.38 and 1.414) in muscle, [29], heavy intrinsic autofluorescence, shallow imaging depth of these techniques and sub-optimal labelling densities have limited their utility for 3D super-resolution mapping of nanodomains.

Recent developments have presented a few potential solutions. Combination of adaptive optics,[30] structured illumination (SIM)[31] or light-sheet techniques[32] with 3D single marker localisation approaches have yielded sub-50-nm axial resolution whilst preserving in-plane super-resolution. An alternative approach is the principle of expanding the fluorescence marker topography of a labelled sample using a self-expanding hydrogel, called Expansion Microscopy (ExM) [33]. This allows features which were smaller than the diffraction-limited resolution of the microscopes to be resolved with no additional optical modifications or marker localisation protocols. The departure from localisation microscopy, compatibility with traditional far-field imaging techniques (e.g. confocal microscopy) and conventional marker probes (with protocols such as protein-retention ExM)[34] have allowed biologists to consistently achieve a resolution-improvement by a factor of ~ 4.[34, 35] Combining ExM with STED, SIM or STORM has allowed this improvement to be further enhanced [36-41]. More recent reports have provided refined ExM protocols (called X10 ExM [42] and iterative-ExM[43]) which now allow >10-fold improvement in resolution by improving the volumetric expansion of the sample beyond the standard expansion factor of 4. Over a short period of four years, ExM has been applied in a wide range of studies, such as visualisation of the cytoskeletal and membrane structures of isolated and/or cultured mammalian cells,[35, 44] RNA mapping with the use of expansion-fluorescence in situ hybridisation,[45] detection of pathological biomarkers in human biopsy tissues,[46] neural circuitry in whole brains,[47] microbial systems ,[38, 44] and model organisms[41, 48-51]. Such diversity in applications underscore a number of key improvements that have been made to the hydrogel and probe chemistries, and the protocol of expansion[34] which makes the principle of ExM adaptable for a range of cell and tissue types. The more recent applications of ExM for making highly-precise measurements on true molecular-scale structures (e.g. 3D tubulin organisation in centrioles,[52] and subunit organisation of the nuclear pore complex[53]) now present this technique as a validated tool for making nanometre scale measurements.

We aimed to develop an approach, based on ExM, to resolve not only the positions of the individual RyRs, but also their individual chemical identities (site-specific phosphorylation) in cardiomyocytes. This paper describes how we combined X10 microscopy with Airyscan (a protocol which we call “enhanced expansion microscopy” or EExM) to achieve a working resolution which we estimate to be ~ 15 nm in-plane and ~ 35 nm axially. We have exploited this 3D super-resolution to map both the positions and the phosphorylation state of RyRs within the three-dimensionally-complex nanodomains, both at the surface and interiors of cardiomyocytes at single-protein precision. This approach has revealed nanometre-scale re-arrangements of individual RyRs, deterioration of nanodomain sizes and the spatial patterns of phosphorylation of RyR (at the residue Ser2808, which enhances RyR excitability and open probability)[54] in cardiomyocytes of a rodent model with right ventricular failure. We detail how this level of positional and biochemical information of individual RyRs can be exploited for *in silico* inquiry of the structural basis of nanodomain Ca^{2+} signalling at a spatial and temporal resolution which has never been achieved experimentally.

Results

Evaluation of EExM for super-resolution imaging of cell interior

For evaluating expansion microscopy as a method for imaging cell interiors, we examined lattices of α-actinin called ‘z-discs’ (red-hot; Fig 1A) and networks of microtubules (green) in the interior of cardiac muscle cells. The highly uniform α-actinin lattices and their span across the entire width of the cell (15-

30 μm in thickness) made the z-discs a useful intrinsic standard for comparing the resolution of deconvolved confocal microscopy, 2D dSTORM (under HiLo oblique illumination)[55], DNA-PAINT (in TIRF), 4x EExM and 10x EExM (Fig 1B, left to right). In longitudinal view of the cells, each modality revealed a highly regular z-disc arrangement. Magnified views showed a double-banded morphology within each z-disc which was resolvable only with DNA-PAINT, 10x EExM and, to a lesser extent, with 4x EExM (Fig 1C). Line profiles of the α-actinin distribution across the z-discs (as indicated in Fig 1C) in each type of data (Fig 1D) revealed three key observations: The higher resolution techniques (e.g. dSTORM compared to confocal) generally reported the α-actinin lattices to be narrower. Despite offering in-plane resolution comparable to 4x EExM (~ 40-50 nm), dSTORM did not detect the double-banded morphology of α-actinin. Intensity profiles of DNA-PAINT images were virtually identical to those acquired in the cell interior with 10x EExM. The longitudinal separation between the peaks (illustrated in red in the right panel of Fig 1D) was very similar between DNA-PAINT and 10x EExM (Fig 1E; Means: 74.0 vs. 70.1 nm). This confirmed that the resolution achieved in these two modalities are comparable (we estimate ~ 15 nm in-plane). Based on a contemporary model of the cardiac z-disc featuring up to six longitudinally-arranged parallel lattices of α-actinin[56] (Fig 1F), we simulated a likely antibody (Ab) labelling pattern in these cells (supplementary Figure S2). A double-banded morphology closely mimicking the experimental data was observed when DNA-PAINT and EExM images of a gradient of Ab penetration at the z-disc lattice were modelled. The simulation confirmed that the principal determinants of the observed labelling pattern were the effective lateral and axial resolution of ~ 15 and 35 nm respectively (supplementary Figure S3).

To demonstrate the enhancement that 10x EExM offers in imaging cell interiors, we illustrate the nanoscale 3D relationship between the α-actinin lattices of the z-discs (grey) and the microtubule network (colour-coded 3D geometry traced by α-tubulin in Fig 1G; magnified view in 1H) throughout a 5 μm-thick volume of the cell, at a depth of ~ 5 μm from the cell surface. A line profile illustrates how two intertwined microtubule bundles (black line) are tessellated at ~ 50 nm of the two outer layers of the α-actinin lattices of the z-disc. We used the regularity of the z-disc spacing (a feature known as 'sarcomeric length'; SL) along the length of the cell to confirm isotropy of expansion in these hydrogels (supplementary figure S4A-C). The consistency in the double-banded morphology in α-actinin labelling was used as evidence that the spatial measurements were unaffected by gel-to-gel variations in the expansion factor (supplementary figure S4D-F).

RyR arrays within intracellular nanodomains resolved with 10x EExM

The RyR organisation within near-surface nanodomains was examined with 10x EExM and compared with DNA-PAINT as the current benchmark.[20] A clustered labelling pattern was observed across the surface regions visualised with both techniques (Fig 2A-i). In magnified view, 10x EExM revealed punctate labelling densities (Fig 2A-ii) with strong resemblance to the patterns seen in DNA-PAINT. In dSTORM images at depths of ~ 10 μm inside the cells, the RyR labelling appeared more clearly banded (Fig 2B-i). Closer examination of both dSTORM and 10x EExM data revealed clusters which were curved and/or elongated (Fig 2B-ii), however dSTORM data did not reveal any sub-structure within the cluster regions (left). The 10x EExM images reported a punctate labelling morphology of RyRs (right), similar to that seen near the cell surface. With a simulation, we established that the punctate appearance of clusters was enabled by, and consistent with the superior in-plane and axial resolution offered by 10x EExM of ~ 15 nm and 35-40 nm respectively (supplementary figure S5). A maximum-intensity projection of RyR labelling, colour-coded for depth throughout a 1-μm-deep cell volume, illustrates the complexity of the 3D topography of RyRs visualised now with 10x EExM (Fig 2C). Fig 2D-i illustrates the flat

topology of cell surface RyR arrays (left) with 3D isosurface visualisation (middle), colour-coded for the axial (z) depth. This topology was consistent with an RyR (orange in schematic, Fig 2D-i, right) alignment that is parallel to the surface plasmalemma (cyan). The RyR clusters in the cell interior regions (maximum-intensity projections in Fig 2D-ii and -iii, left) revealed nanodomains which curved around local t-tubule membranes. Depending on whether the cluster was imaged either end-on (Fig 2D-ii) or side-on (Fig 2D-iii), relative to the image planes, the depth-encoded 3D visualisation showed distinct gradation of the colours of the isosurface (Fig 2D-ii & -iii, middle). The approximated orientations of the RyR array (orange) and the tubular plasmalemma (cyan) are shown schematically on the right.

For further analysis of the positions of the punctate RyR labelling densities, we used an algorithm which determined the *in situ* 3D centroids of each RyR punctum. Supplementary Fig S5 visually illustrates the RyR puncta of a curved cluster and their corresponding 3D centroids. The spatial organisation of these puncta (see 3D data in supplementary figure S6) were similar to the selection of 3D-rendered tomographic EM data published previously from rat cardiomyocytes.[14] In the interior clusters, an approximately exponential distribution of RyR cluster size was observed (Fig 2E, main panel; mean of ~ 8.23 RyRs/cluster). Many of the puncta were observed either as solitary or small (< 5 RyRs) clusters both in the cell interior and near-surface regions. The cluster sizes in the cell interior strongly resembled the size distribution in near-surface nanodomains (mean of ~ 8.98 RyR/cluster; Fig 2E, inset). A dot-plot analysis illustrated that the counts of RyR in each near-surface cluster were very similar between the 10x EExM and DNA-PAINT data (mean ~ 7.84 RyR/cluster; blue in Fig 2E inset). We further examined the RyR assembly pattern in larger (≥ 4 RyRs) clusters with histograms of the nearest neighbour distance (NND; blue in Fig 2F) and the average distance between the 3 nearest neighbours for each RyR (3ND; red in Fig 2F). The NNDs, a measure of the co-clustering between individual receptors, followed an approximately-Gaussian distribution with a mean of ~ 45 nm which was consistent with previous measurements of centre-to-centre spacings between RyRs made with tomographic EM.[13] The 3NDs, reporting the average spacings between RyRs in a given array, were more variable and produced a histogram with a rightward tail and a mean of ~ 73 nm. This contrasted with the 3NDs histogram for near-surface nanodomains (grey barplot overlaid with the interior 3ND histogram, shown in green, in the inset of Fig 2F) which showed less variability and a shorter tail (mean ~ 64 nm). The NND and the 3ND distributions for near-surface clusters provided an additional point of comparison between the measurements between DNA-PAINT and 10x EExM and showed that the shapes of the two distributions were independent of the method (supplementary figure S7).

Adaptation of EExM for visualising RyR re-arrangement in pathology

RyR clusters are susceptible to remodelling, particularly in pathologies of the heart such as atrial fibrillation.[8] Exploiting the enhanced resolution of 10x EExM, we examined changes in the structure of RyR nanodomains in right ventricular (RV) myocytes of rats displaying RV failure, following treatment with monocrotaline (MCT). At the cell surface the clustering pattern of RyR labelling was broadly comparable between control (Fig 3A) and MCT-RV cells (Fig 3B), however, solitary puncta were more abundantly observed in the latter (arrowheads). Compared to control cells (Fig 3C), RyR clusters near the surface of MCT-RV cells (Fig 3D) visually appeared smaller; many regions contained single puncta. Closer examination allowed us to characterise, for the first time, changes *within* the nanodomains which accompany this pathology. In the interiors of both MCT-RV and control cells, the RyR clusters followed a more banded organisation which reflected the organisation of the sarcomeres (Fig 3E & F). However, clusters in MCT-RV were more compact and contained visibly fewer RyRs (Fig 3G & H).

To assess the nature of the mutual re-organisation of RyR channels, we compared the NNDs and the 3NDs of RyRs in the larger clusters (≥ 4 RyRs) of control and MCT-RV cells. In contrast to the narrow

unimodal NND distribution for RyRs in interior nanodomains of control cells (mode ~ 40 nm; Fig 3I, blue), the MCT-RV NND distribution (grey, overlaid) featured two peaks at ~ 45 nm and ~ 90 nm respectively. A similar trend was observed in RyRs in near-surface nanodomains of MCT-RV cells (supplementary figure S8). This observation suggested that at least a small subset of RyRs had dissociated from their default clustering pattern. This hypothesis was further supported by the longer rightward tails observed in the 3ND histograms (Fig 3J and S7), which related to RyR clusters with looser arrangement of receptors.

Confirming the visual observations of smaller RyR clusters, coupled with higher abundance of solitary RyRs in MCT-RV, we observed an ~ 40% reduction in the mean number of RyRs in MCT-RV clusters compared to control in both cell interior and near-surface nanodomains (Fig 3K). The smaller cluster size is also compatible with the hypothesis of nanodomain fragmentation during the disease (Fig 3L), leading to greater variability in the RyR-RyR distances.

Mapping phosphorylation status of RyRs

In addition to spatial remodelling, RyR nanodomains are also known to undergo types of biochemical remodelling both in healthy physiology and in disease. These include the phosphorylation of RyR at Ser2808. With two-colour 10x EExM, we mapped the Ser2808 phosphorylation state of RyR (with an anti-pSer2808 Ab; purple in Fig 4A) relative to the positions of individual RyRs (grey) in near-surface and interior nanodomains of rat cardiac muscle cells. Magnified views of both types of nanodomains showed that punctate pSer2808 labelling densities either overlapped or closely tessellated with RyRs consistently (Fig 4B). These data (inset, Fig 4C) were used to localise the centroids of the RyR (grey circles) and pSer2808 puncta (purple). Individual RyRs were recorded as 'phosphorylated' if their centroid consisted of any detectable pSer2808 labelling within a 30-nm 3D radius (Fig 4C). Approximately 1-3% of the pSer2808 puncta were not detected in association with RyRs (arrowhead).

We visually compared the localisations of RyRs which were phosphorylated at Ser2808 within near-surface nanodomains of control and MCT-RV cells (Fig 4D & E respectively) to find that only a subset to be phosphorylated. As a point of comparison, we examined the pSer2808 labelling at the near surface nanodomains in control cells which were stimulated with electrical pacing and the β-adrenoceptor agonist isoproterenol, which is known to evoke acute intrinsic hyperphosphorylation of the RyRs.[57] The densities of pSer2808 labelling in these RyR clusters were noticeably higher (supplementary Figure S9). In cell interior nanodomains (Fig 4F & G), the density of pSer2808 labelling appeared visually comparable for control and MCT-RV cells. Given that RyR clusters were smaller in MCT-RV, the visually identifiable proportion of phosphorylated RyRs was higher in these cells. Histograms of the proportion of phosphorylated RyRs in each cluster (containing ≥ 4 RyRs; P_{phos}) between control (purple; Fig 4H) and MCT-RV (blue) cells were comparable (mean ~ 0.31 for control and ~ 0.30 for MCT-RV) and consisted of similar modes (~ 0.24 and ~ 0.28 respectively). Few clusters featured either no or complete phosphorylation. A similar distribution was observed for cell interior nanodomains of control cells (purple in Fig 4I; mean ~ 0.27 and mode ~ 0.16); however, the distribution for P_{phos} in MCT-RV cells was right-shifted (blue; mean ~ 0.45 and mode ~ 0.42). This shift in P_{phos} closely mimicked the shape of the equivalent histogram analyses performed on near-surface and interior RyR clusters of control cells (insets of Fig 4H&I) which were stimulated with isoproterenol and electrical pacing (means ~ 0.42 and ~ 0.57 respectively).

To investigate whether the likelihood of RyR phosphorylation was dependent on the location within the nanodomain, we plotted the density of pSer2808 puncta against the distance from the edge of the RyR cluster. A near-uniform density was observed in regions ≥ 50 nm inside of the cluster-boundary of

control cells (purple; Fig 4J). In a simulation, we observed that such a uniform density profile is consistent with a random uniform probability of RyR phosphorylation throughout the cluster (supplementary figure S10). This density profile appeared to be uniformly amplified by a factor of ~ 2 when control cells were stimulated as above (grey; Fig 4J). However, in MCT-RV cells, the pSer2808 puncta density showed a distinct gradient extending from the cluster boundary to the centre. This density-distance analysis suggested that healthy cells, when under higher β-stimulation, allow uniform increase in RyR phosphorylation at Ser2808 throughout each nanodomain (Fig 4K-i & ii). Despite nanodomains being smaller and/or fragmented, they typically foster a higher density of phosphorylated RyR at the centre of the clusters in MCT-RV cells (Fig 4K-iii).

Simulation of nanodomain calcium dynamics

Given the positions of individual RyRs and their respective phosphorylation state, we investigated the likely spatiotemporal patterns of Ca^{2+} release in these nanodomains determined purely from these structural considerations. Two spatially-discretised models based on the RyR and pSer2808 data of flat, approximately median-sized near-surface nanodomains were constructed – one from control (Fig 5A) and the other from MCT-RV (Fig 5B). The centroid positions of each RyR (circles Fig 5C&D) and the phosphorylation identity (yellow for phosphorylated) were marked in each example. 10 independent simulations of the temporal pattern of the local cytoplasmic [Ca^{2+}] in the nanodomain cleft in Ca^{2+} signals (known as 'Ca^{2+} sparks') were performed for control (Fig 5E) and MCT-RV (Fig 5F) examples. The control cluster consistently gave rise to sparks with amplitudes of 30-80 μM [Ca^{2+}]. By comparison, the MCT-RV nanodomains featured Ca^{2+} release which lacked the temporal synchronisation and development into the full temporal profile of sparks (also see supplementary movie). The simulated image series of [Ca^{2+}] in the control (Fig 5G) and MCT-RV (Fig 5H) nanodomains allowed visual examination of likely spatiotemporal pattern of Ca^{2+} release at resolutions of 10 nm and 0.1 ms. In control nanodomains, we often observed Ca^{2+} release which was seeded by individual or sub-groups of phosphorylated RyRs in the earliest phases of the spark (i.e. at ~ 10-20 ms; Fig 5G-ii). These events appeared to cumulatively recruit their nearest neighbours (Fig 5G iii-vi) via CICR, typifying the 'triggered saltatory' mechanism of initiating Ca^{2+} sparks hypothesised previously.[18] A similar triggering was observed in MCT-RV clusters (Fig 5H-ii); however, the recruitment of their neighbouring RyRs was neither cumulative nor complete. Dephosphorylation of the RyRs in the MCT-RV example whilst maintaining all other parameters showed complete failure of the nanodomain to release Ca^{2+} (supplementary movie). This suggested that RyR hyperphosphorylation at Ser2808 could serve to offset the loss of the nanodomain's excitability during RyR re-arrangement.

Discussion

10x EExM has allowed us to map the 3D positions of dyadic RyRs in nanodomains deep within the interiors of cardiomyocytes with a resolution which matches that offered by DNA-PAINT for imaging 2D nanodomains at the cell periphery.[20] This advancement is enabled by a superior in-plane and axial resolution over existing benchmarks such as 3D dSTORM data published recently.[22] With this, we have observed both acute and chronic changes in the phosphorylation of the RyRs within the nanodomain and molecular-scale re-positioning of RyRs coinciding with the RV failure pathology.

ExM as a quantitative true-molecular-scale imaging technique

Our implementation of 10x EExM is its first application to examine the components of Ca^{2+} nanodomains, particularly in the cell interior. We have demonstrated its superior resolution compared to

established imaging techniques such as dSTORM and 4x EExM (Fig 1B&C) by mapping 3D cytoskeletal components in cardiomyocyte interiors. With near-surface imaging of both α-actinin lattices and RyR clusters, we showed that the resolution achieved by 10x EExM almost matches that of DNA-PAINT.[20] A notable gain in combining the X10 microscopy protocol of Truckenbrodt *et al* [42] with 3D Airyscan is a distinct improvement in the axial resolution to ~ 35 nm. Simulations of the 10x EExM imaging process using two models of curved nanodomains – one of a large RyR cluster and the other of a cluster with a narrower radius of curvature (supplementary figure S5) – have confirmed that the 10x EExM imaging protocol is particularly suited for imaging RyRs (spaced ~ 40 nm apart) within curved nanodomains. They revealed that the detection accuracy of single RyRs was better where the working resolution was ~ 15 nm in-plane and ~ 35 axially. Accuracy of aligning fine structures in the image with multi-channel 10x EExM is further subject to chromatic alignment of the imaging channels. With the Airyscan imaging system that we used, we found that this alignment error was 10-13% of the effective resolution achieved (see Methods sub-section on estimation of the point spread function and effective resolution for details).

As an imaging protocol, 10x EExM was difficult to master initially due a drop in the RyR labelling intensity equivalent to the cube of the expansion factor. However, four key features of our experimental design permitted the single-RyR level of sensitivity to be achieved during the imaging. Firstly, the digestion and removal of the cell material in ExM renders the RI of the sample homogeneous as described before.[37] Whilst dSTORM experiments for mapping RyR[23, 24] used an 80% glycerol mounting medium to reduce the intracellular RI inhomogeneities, no active clearing approach such as this was adopted. Secondly, the clearing also led to a near-complete removal of the autofluorescence arising from the intrinsic contractile proteins, mitochondrial NADPH and flavin co-enzymes, which occupy > 40% of the cardiomyocytes' cytoplasmic volume (discussed by Larcher *et al*)[58]. For EExM, this enhanced the detection of low marker densities substantially. This was a clear advantage over our previous DNA-PAINT and dSTORM experiments[18, 20] where marker localisation accuracy was limited considerably by cellular autofluorescence.[59] Thirdly, our selection of bleach resistant fluorophores, Alexa488 and Janelia549 in particular, also allowed greater consistency in retention and detection of RyRs during the highly oxidative gelation step of ExM[42] and Airyscan imaging respectively. Finally, the choice of the Airyscan method over confocal microscopy for imaging the sample further enhanced the effective resolution-improvement and greater photon collection efficiency enabled by its sensitive array detector and the absence of a physical pinhole.[60]

To validate 10x EExM as an accurate tool for measuring intracellular structures, we performed two key tests to confirm that (i) the expansion of the cellular structures was isotropic and (ii) the effect of gel-to-gel variations in expansion factor (~ 7-10.5) on the standard deviation of the measurements was minimal (supplementary Fig S4). There are no ideal calibration standards (e.g. DNA-origamis which would expand in proportion to the structures of interest) for these tests currently; however, we used the periodicity of the myocytes' sarcomeres and fixed-width of z-discs as intrinsic reporters of local gel expansion. The standard deviation of < 10% was well in the range of the biological variations of these structures observed previously[61], providing us with assurance on the above requirements. The similar measurements in the cluster size (Fig 2), NND and 3ND (supplementary Fig S7) between DNA-PAINT and 10x EExM provided additional confirmation that the spatial calibrations of the expansion factor and the isotropy of expansion translate well to the scale of RyR clustering (~ 30-80 nm). As a super-resolution approach for examining and quantifying structures with 3D complexity, therefore, 10x EExM presents a useful and highly reproducible technique. A comparison with respect to the ease of use of 10x EExM versus high-end localisation microscopy methods does not allow a clear-cut conclusion. The 5-day sample preparation protocol and an as yet unproven suitability for examining tissue, particularly heart tissue

containing high densities of collagen[42], are still limiting factors that can reduce the practicality of 10x EExM for some experimental settings. On the other hand, the purely chemical approach of EExM is likely more accessible to cell biologists who often have limited expertise in instrumentation development and the intricacies of fluorophore photochemistry, as argued previously.[62]

3D and chemical topography of nanodomains

By applying 10x EExM to image RyR labelling in rat ventricular myocytes, we observed puncta, whose identities as single RyRs have been confirmed both visually (benchmarking against DNA-PAINT; Fig 2A)[20] and quantitatively (by cluster sizes and RyR NND and 3ND measurements; supplementary Fig S7). The RyR arrays patterns observed with both methods are irregular and, therefore, are consistent with the non-crystalline cluster self-assembly which we proposed previously based on near-surface DNA-PAINT data (see supplementary figure S2-B of [20, 63]). The 10x EExM data are the first optical 3D data of fully-resolved RyR patterns in interior nanodomains. This direct approach to RyR counting made the *in situ* analysis of RyR clustering more straightforward than indirect protocols (based on event density[22, 24] or frequency[20] calibrations) used in dSTORM and DNA-PAINT experiments previously. The superior 3D data have allowed clear visualisation of the non-planar topology of interior nanodomains at an unprecedented level of detail (Fig 2D and S5). These data have allowed the first optical comparisons between the fine structure of near-surface and interior nanodomains. Overcoming the uncertainties in RyR counting with techniques like dSTORM[18, 23], the 10x EExM data suggest that the two types of nanodomains are similar in size and receptor organisation pattern (confirmed by measurements of NND).

An advantage of the multicolour capability of ExM is the ability to map, for the first time, the phosphorylation state of the individual RyRs *in situ*. The anti-pSer2808 is a well-established antibody and has been used extensively to characterise physiological[64, 65] and pathological[66] RyR phosphorylation. In our analysis, we observed that ~ 30% of the RyRs are phosphorylated at Ser2808 at the basal (unstimulated) state. Direct comparisons of the cluster-specific P_{phos} between near-surface and interior nanodomains provided both visual and quantitative evidence that basal level phosphorylation at Ser2808 is comparable between the two cellular regions. It is well characterised that Ser2808 can be modified primarily by protein kinase A (PKA) but also by calmodulin kinase II (CAMKII),[67] commonly under the control of intracellular signalling cascades downstream of β-adrenergic stimulation, to enhance the RyR open probability. The local densities of pSer2808 measured throughout the near-surface nanodomains in control myocytes (Fig 4J) may therefore reflect a basal 'tuning' to maintain near-uniform local excitability of RyRs throughout the nanodomain. In an additional iterative simulation which artificially inverted the RyR phosphorylation pattern (supplementary Fig S11), we observed a higher-than-normal likelihood of the nanodomain to ignite full-blown Ca^{2+} sparks, originating from the locations of pSer2808. This suggested to us that the nanodomain's basal pSer2808 tuning may encourage a uniform profile of RyR excitability throughout the nanodomain, potentially as a counter against geometrically-determined heterogeneity, proposed in previous models.[21] We note that the excitability of individual RyRs are functionally regulated by multiple phosphorylation sites on each of the four RyR subunits, physical interactions with regulators such as FK506 binding protein 12.6 [68] and junctophilin-2 [69] on their cytoplasmic domains. Mapping all of these regulators simultaneously may not be achievable given the bulky size (and potential steric competition) of current probes; however, this would enable a more comprehensive simulation of the intra-nanodomain heterogeneities in RyR excitability.

We recognise that the *in situ* P_{phos} values estimated for larger nanodomains through our imaging data (Fig 4H&I; ~ 30% for control myocytes) are lower than that reported by Western Blot analysis of denatured cardiac homogenates using the same antibody (~ 69%) [70]. The differences in the measurements are not

clear, but likely to be methodological, either relating to potentially-incomplete labelling of pSer2808 *in situ* or an unaccounted selectivity to phosphorylated RyRs in the membrane fractionation methods used in *in vitro* studies.[70] We note that the proportional increase in P_{phos} (by ~ 50%) that we see under β-adrenergic stimulation (with electrical pacing in the presence of isoproterenol) closely reproduces the *in vitro* measurements on pSer2808 made by Huke & Bers.[65]

Modification and redistribution of ryanodine receptors in physiology and pathology

Ser2808 is only one of a handful of PKA and CAMKII targets on the RyR[67] and it is possible that there is little/no relationship between RyR self-assembly pattern and pSer2808. In our experiments, control cells undergoing stimulation showed uniform phosphorylation of RyR throughout the nanodomain and there was no detectable difference in phosphorylation pattern between near-surface and interior nanodomains. RyR phosphorylation patterns appear different in MCT-RV cells. Interior nanodomains preferentially show hyperphosphorylation at the basal state. The higher systemic β-adrenergic stimulation experienced by these animals[71] and the chronic (over a few weeks) upregulation of PKA expression in MCT-RV cells[72] could well explain this observation. The exclusivity of this phenotype to interior nanodomains however contrasts clearly with the acute effects of β-adrenergic stimulation observed in control cells. This may simply reflect the broad changes in β-adrenergic intracellular signalling mechanisms which accompany the disease.[72] Despite the preservation of P_{phos} in peripheral nanodomains, a redistribution of pSer2808 is seen (Fig 4J&K). This may be the likely result of an unravelling nanodomain membrane structure which can allow (i) a spatial redistribution of the AKAP scaffold proteins which harbour PKA within the nanodomain[73], (ii) increased access of phosphatases to the peripheral regions of the nanodomain, (iii) or both.

In pathology, we observe a remodelling of the nanodomains which feature a less closely packed RyR-RyR pattern with increased inter-receptor distances, both near the cell surface and in interior regions. This change appeared to be most prominent in the cardiomyocytes of the RV. NND and 3ND measurements in the LV (column 4 of supplementary Figure S7), by comparison, more closely resembled the distributions in the control cells. The curvatures and the extended shapes of the RyR cluster in the cell interior were less apparent. The superior resolution of 10x EExM has provided a first true molecular-scale view of the RyR cluster fragmentation, first reported very recently[74] using STED and dSTORM at resolutions of 40-80 nm. The 10x EExM data presented in Fig 3 therefore report the smallest spatial scale at which pathological remodelling of heart has been observed to-date.

Simulation of nanoscale signalling based on super-resolution data

The simulation (Fig 5) developed from 10x EExM is the first model of intracellular Ca^{2+} signalling which captures experimentally-determined positions and biochemical state of individual RyRs. In Fig 5E&F we demonstrate its utility, particularly in examining one of the nanodomains' fundamental features – the ability to produce fast and reproducible Ca^{2+} sparks. Direct comparisons of the control RyR arrangement with the disease phenotype relative to the Ca^{2+} revealed the diminishing coupling between adjacent RyRs as they are dispersed. This manifested in both failed Ca^{2+} sparks as well as unsynchronised opening of individual RyRs within the nanodomain (Fig 5H). Whilst the diminished amplitude of the sparks may be explained by the smaller number of receptors in the diseased nanodomains, the higher variability in the likelihood of evoking a full Ca^{2+} spark is striking (Fig 5F). Failed Ca^{2+} sparks in this spatial scale are unlikely to be detectable with the current state-of-the-art Ca^{2+} imaging techniques which have to contend with a number of limitations which associate contemporary Ca^{2+} imaging methods. These limitations include high resting cytoplasmic [Ca^{2+}], diffusion of Ca^{2+} indicator dye as well as Ca^{2+}, poor photon

efficiency particularly when using a pinhole-based detector and the diffraction limited resolution of the imaging system.[75] Spatially accurate models such as this are therefore a useful approach to studying the functional phenotype of nanodomain signalling in disease.

Limitations

Our application of 10x EExM has come with a few noteworthy limitations. Whilst we characterised the isotropy of expansion and reliability of the expansion factors estimated in the scales >70 nm, we were limited by the lack of a known calibrant in the range of 10-30 nm. Cross-validation of RyR NND measurements against DNA-PAINT was a useful workaround; however, a DNA-origami (which, at present, has been proposed in a pre-print manuscript)[76] or similar spatial calibration standard which reports the gel expansion in this spatial scale is needed. For now, we find assurance in our approach which is similar to the analyses performed by others using features of intrinsic ultrastructures (e.g. the circularity of the cross-section of centrioles).[52] The single RyR positions detected from the 3D 10x EExM data were likely to be limited by two factors. The poorer axial resolution which, as we demonstrate in the 3D simulation, could lead to errors or loss of detection in ~ 5% of the receptors, particularly in regions where RyRs are aligned orthogonal to the image-plane (supplementary Fig S5). Achieving ~ 10x expansion is an important determinant because we show in the same simulation that approximately halving of this effective resolution leads to ~ 30% drop in the detection accuracy. Secondly, the binding efficiency of the antibody probes is likely to be limiting. Whilst RyR counts within clusters were comparable to those achieved with DNA-PAINT (and two different Abs) previously,[20] there may be steric limitations in the Abs' access to the targets. The RyR and/or pSer2808 positions may be subject to offsets dues to the size of the Ab markers relative to the effective resolution of the data, hence we required a distance-based likelihood criterion for determining the identity of the RyRs carrying the detected phosphorylation. Probes that are more compact, but compatible with the pro-ExM chemistry should be examined in the future as a solution to this.

We have used flat, near-surface nanodomains in our simulations to exploit the certainty of the two-dimensional geometry of cytoplasmic Ca^{2+} diffusion. One of the main limitations in the 10x EExM images of RyR and pSer2808 is the lack of an independent marker of the curvature of the t-tubular membranes[62] which determines the 3D diffusion of Ca^{2+} both within and beyond the nanodomain. This is a limitation particularly in MCT-RV cells where the t-tubular system broadly undergoes remodelling[77] and there is visual evidence in the 10x EExM data of diminishing curvature of the nanodomain. Future investigations therefore would benefit from establishing reliable plasmalemmal and SR markers compatible with ExM. Furthermore, the simulations utilised a general description of RyR dynamics and phenomenological implementation of phosphorylation. Future detailed modelling studies would benefit from biophysically detailed species- and disease-specific formulations of these model components; results presented occurred within parameter ranges which illustrated the differences between control and MCT, but do not necessarily translate to those which may manifest physiological behaviour. These simulation results should therefore be considered as a demonstration of the potential for the structural data attained to be used in future mechanistic studies rather than rigorous analysis of the effect of MCT remodelling on cardiac CICR. Nevertheless, these data indicate an important role for nanodomain structure in regulating EC coupling, illustrating that the number of RyRs, their spatial distribution, and both the proportion and distribution of phosphorylation sites can all have an impact on local Ca^{2+} dynamics and inducibility of CICR; all these factors are observed to be remodelled in MCT and potentially other disease models.

Methods

Cell preparation and animal models

Live myocytes were isolated from hearts freshly dissected from Wistar rats, euthanised according to a protocol approved by the UK Home Office. Pulmonary arterial hypertension (PAH) was induced in 5-week old adult rats with a single intraperitoneal injection of monocrotaline (MCT; Sigma-Aldrich) as detailed previously.[78] RV-failure was typically observed between days 21 and 28, when the animals were euthanised (references to these cell samples are notated as 'MCT-RV' in the text). Isolated right ventricular cells were adhered to coverslips as described before[20] and fixed in 2% paraformaldehyde (Sigma) for immunocytochemistry. For examining the effects of stimulating RyR phosphorylation, living cells were simultaneously stimulated with electrical field stimuli at 1 Hz and 100 nM Isoproterenol (Sigma) dissolved in Tyrode's solution prior to fixation. See supplemental experimental procedures for more a detailed protocol. Data presented in this manuscript included cells isolated from 4 control animals and 5 MCT-treated animals. Sample numbers stated in the text refer to cell numbers considered in each analysis.

EExM

ExM was performed on fixed and stained cell samples either according to the proExM protocol for 4x expansion[34] or X10 microscopy protocol.[42] Immunofluorescent labelling protocol is detailed in the Supplementary information. pSer2808 was labelled with anti-RyR2-pSer2808 IgG (A010-30AP, Badrilla Ltd, UK). Among the secondary Abs that we tested, we chose goat anti-mouse and goat anti-rabbit conjugates of AlexaFluor488 and JaneliaFluor549 for their strongest photostability during the ExM protocol and shorter wavelength of emission, conducive for superior imaging resolution. The labelling patterns seen with these Abs were also visually confirmed by ExM samples labelled with longer-wavelength secondary Ab (conjugates of Atto 647-N). Samples were subjected to confocal or Airyscan imaging on an inverted LSM880 with Airyscan (Carl Zeiss, Jena) was used with a Plan-Apochromat 63x 1.4 NA objective with a working distance of 0.19 mm. Image sampling was set to < 40 nm/px in x-y plane and 100 nm in z. The true spatial scale of the images were calculated by multiplying the voxel sampling by the linear expansion factor of the given gel (estimated as detailed in supplementary Figure S3E). All distances reported in the Results and Discussion sections from ExM data are based on these rescaled distances.

DNA-PAINT and dSTORM of immuno-labelled cells was performed as detailed in previous reports,[20, 24] on a custom-built Nikon TE2000 TIRF microscope equipped with a 60x 1.49 NA TIRF objective and a 671 nm diode laser (Viasho, China). For dSTORM, the beam angle was inclined to achieve HiLo illumination,[55] focused deeper into the sample. Primary DNA-PAINT and dSTORM data were recorded with an Andor Zyla-5.5 sCMOS camera (Andor, Belfast) using the freely-available Python Microscopy Environment (PyME) software (www.python-microscopy.org). PYME was used for localising the fluorophore positions and rendering the point data of dSTORM and DNA-PAINT experiments onto 5 nm and 1 nm pixel grids for further spatial analyses.

See supplemental experimental procedures for more details on imaging protocols.

Spatial analysis of EExM and DNA-PAINT data

Segmentation: Local ensembles of punctate RyR densities were segmented into cluster regions on a binary mask using a protocol used previously for segmenting DNA-PAINT images.[20, 24] These masks

were used for the distance-based analysis (Fig 4J) of labelling density using a Euclidean distance transform of the cluster area as detailed before.[79]

Detection: Punctate labelling densities which were typical for RyR and pSer2808 Ab labelling in EExM and DNA-PAINT data were analysed by their spatial distribution. A detection algorithm, similar to that used previously,[20] was implemented in Python to record the three-dimensional coordinates of the centroid of each punctum; each punctum was approximated as a single RyR, as before. [20] For cell surface (2D) DNA-PAINT and 10x EExM data, the detection was 2D. A 3D implementation of this was used for mapping RyR and pSer2808 puncta in the cell interiors. Please see supplemental experimental procedures for a detailed protocol. To measure the longitudinal separation between the double peaks of α-actinin, the sub-pixel centroids of each intensity peak was calculated using a Gaussian line profile fitting procedure detailed previously.[61, 80] The average distance between the two centroids was calculated for each line (as plotted in Fig 1D).

Estimation of the point spread function and effective resolution: The PSF for the confocal deconvolution was estimated by acquiring and averaging between 3D confocal z-stacks of 100 nm yellow-green or red-orange Fluospheres (ThermoFisher) immobilised inside a 2% agarose gel at a depth of ~ 20 μm from the coverslip. To estimate the effective PSF of Airyscan post-processing 3D image-data, 20 nm yellow-green Fluosphere beads were imaged within a 2% agarose gel and subjected to the same analysis. The effective PSF in EExM experiments was estimated by scaling the Airyscan PSF by the expansion factor of the specific sample. Line intensity profiles both in-plane and axial dimensions of the EExM PSF volumes (e.g. supplementary figure S4-B) were fitted with a one-dimensional Gaussian function and the full-width at half-maximum (FWHM) was taken as a close approximation of the resolution. Variations in this FWHM was observed by taking line profiles from beads embedded within the agarose gel at depths of 5, 30 and 47 μm (overlaid in supplementary figure S4-B). These reported in-plane FWHMs of 13.3, 14.8 and 17.3 nm and axial FWHMs of 33.4, 39 and 46 nm at these depths respectively.

The estimated PSF is subject to two principal uncertainties. These include the error in localising the centroids of the bead images prior to averaging (with bead alignment based on a least squares approach, we estimate that this associates a broadening of the estimated PSF < 1.5%). Further, potential shift variances in the PSF when sampling beads in different locations of the sample would have led to a broader PSF. In the bead data acquired, we did not observe major differences in the bead images from different regions (laterally) within the imaging field which could not be explained by noise or sub-pixel-scale drift of the beads.

The chromatic alignment of the AlexaFluor488 (green) and JaneliaFluor549 (red) emission channels was important for accurately localising the pSer2808 signatures of RyRs. We assessed this alignment by acquiring the Airyscan images of hydro-gel embedded 100-nm TetraSpeck microspheres (Thermo) in the emission channels under the sample imaging parameters (see supplementary figure S12). Based on this analysis, the spatial error between the channels was estimated to be ~ 10%, subject to the errors in localising the beads which apply to PSF estimation.

Simulation of confocal, dSTORM, DNA-PAINT and EExM images: 3D models of the z-disc (supplementary figures S2 & S3) and the curved nanodomains (supplementary Fig S5) were convolved with a PSF that approximated the resolution achieved by each technique. Confocal and Airyscan PSFs were estimated by imaging 100 nm microspheres in the same imaging conditions as the samples. For 4x and 10x EExM, the Airyscan PSF was upscaled as detailed above. dSTORM and DNA-PAINT simulations used the image simulator of PyME detailed previously.[20]

pSer2808 reassignment: The 3D coordinates of the RyR and pSer2808 labelling puncta were detected independently (in their separate channels of the two-colour data). The RyR puncta which contained a pSer2808 punctum was marked as phosphorylated. Only one RyR was assigned to one pSer2808 punctum.

See supplemental experimental procedures for more details on analysis protocols.

Simulation of the spatiotemporal Ca^{2+} dynamics

To simulate Ca^{2+} dynamics, selected nanodomains were discretised at a resolution of 10 nm and embedded in a 2D grid. Ca^{2+} dynamics within this grid are described by the regular 2D reaction-diffusion equation; L-type Ca^{2+} channel flux was represented by an idealised triangular waveform, and RyR dynamics, controlling intracellular calcium release, were described through a simple 2-state stochastic model. The original *in vitro* study examining the effects of RyR gating kinetics following non-specific phosphorylation of RyRs by Protein Kinase A reported an increase in the RyR open probability by up to a factor of 3.5.[54] To capture an approximate effect of Ser2808-specific phosphorylation in our simulation, the phosphorylated state of the RyR channel was modelled as an increase in the Ca^{2+} sensitivity of the RyRs (by a factor 1.5-3); phosphorylation sites were given either by the imaging data or assigned randomly according the spatial distributions. Simulations were performed over a range of parameters, 10 simulations per condition, with the behaviour of the different geometries and with/without phosphorylation compared under consistent parameter conditions. Equations and parameters are presented in the supplementary material.

Conclusions

The enhancement to the ExM approach has allowed us to map nanoscale features located deeper within cells at a resolution of ~ 15 nm. Exploiting this capability, we have resolved individual RyRs forming three-dimensionally complex clusters within nanodomains in the cell interior. Detection of nanometre-scale changes in position and likelihood of site-specific phosphorylation has allowed us to simulate geometrically realistic spatio-temporal profiles of cytoplasmic Ca^{2+} signals which are encoded by these nanodomains.

Acknowledgements

The authors acknowledge the Wellcome Trust (Seed Award 207684/Z/17/Z awarded to IJ), the Medical Research Council (doctoral studentship awarded to IJ and Strategic Skills Research Fellowship awarded to MAC) for funding. Also acknowledged, is Dr S Boxall of the University of Leeds Bio-imaging Facility for technical assistance and, Dr S Truckenbrodt and Prof D Steele for insightful discussions.

Author contributions

IJ, EW & JC conceived experiments; TMS, MH, RN, YH & LH performed experiments; TMS made primary experimental observations; EP, KKN, ZY & HK provided materials towards primary experiments; IJ, DB & CS wrote the custom code for image analysis and DNA-PAINT/dSTORM image simulation; IJ & TMS performed experimental data analysis, IJ, CS, MAC made the primary interpretation of results, MAC modelled Ca^{2+} signalling, IJ modelled image data; supervision provided by IJ, AJS, JS, JC and CS; primary funding acquired by IJ & MAC.

Supporting Information Available: a Supplementary Information document including supplementary figures, and Supplementary movie 1. This material is available free of charge via the Internet at http://pubs.acs.org.

References

1. Scriven, D.R., P. Asghari, and E.D. Moore, *Microarchitecture of the Dyad.* Cardiovasc Res, 2013. **98**: p. 169-76.
2. Pritchard, H.A.T., P.W. Pires, E. Yamasaki, P. Thakore, and S. Earley, *Nanoscale Remodeling of Ryanodine Receptor Cluster Size Underlies Cerebral Microvascular Dysfunction in Duchenne Muscular Dystrophy.* Proc Natl Acad Sci U S A, 2018. **115**: p. E9745-E9752.
3. Jayasinghe, I.D., M. Munro, D. Baddeley, B.S. Launikonis, and C. Soeller, *Observation of the Molecular Organization of Calcium Release Sites in Fast- and Slow-Twitch Skeletal Muscle with Nanoscale Imaging.* J R Soc Interface, 2014. **11**.
4. Johenning, F.W., A.K. Theis, U. Pannasch, M. Ruckl, S. Rudiger, and D. Schmitz, *Ryanodine Receptor Activation Induces Long-Term Plasticity of Spine Calcium Dynamics.* PLoS Biol, 2015. **13**: p. e1002181.
5. Ouyang, K., H. Zheng, X. Qin, C. Zhang, D. Yang, X. Wang, C. Wu, Z. Zhou, and H. Cheng, *Ca2+ Sparks and Secretion in Dorsal Root Ganglion Neurons.* Proc Natl Acad Sci U S A, 2005. **102**: p. 12259-64.
6. Johnson, J.D., S. Kuang, S. Misler, and K.S. Polonsky, *Ryanodine Receptors in Human Pancreatic Beta Cells: Localization and Effects on Insulin Secretion.* FASEB J, 2004. **18**: p. 878-80.
7. Munro, M.L., X. Shen, M. Ward, P.N. Ruygrok, D.J. Crossman, and C. Soeller, *Highly Variable Contractile Performance Correlates with Myocyte Content in Trabeculae from Failing Human Hearts.* Sci Rep, 2018. **8**: p. 2957.
8. Macquaide, N., H.T. Tuan, J. Hotta, W. Sempels, I. Lenaerts, P. Holemans, J. Hofkens, M.S. Jafri, R. Willems, and K.R. Sipido, *Ryanodine Receptor Cluster Fragmentation and Redistribution in Persistent Atrial Fibrillation Enhance Calcium Release.* Cardiovasc Res, 2015. **108**: p. 387-98.
9. Pinali, C., H. Bennett, J.B. Davenport, A.W. Trafford, and A. Kitmitto, *Three-Dimensional Reconstruction of Cardiac Sarcoplasmic Reticulum Reveals a Continuous Network Linking Transverse-Tubules: This Organization Is Perturbed in Heart Failure.* Circ Res, 2013. **113**: p. 1219-30.
10. Sun, X.H., F. Protasi, M. Takahashi, H. Takeshima, D.G. Ferguson, and C. Franzini-Armstrong, *Molecular Architecture of Membranes Involved in Excitation-Contraction Coupling of Cardiac Muscle.* J Cell Biol, 1995. **129**: p. 659-71.
11. Franzini-Armstrong, C., F. Protasi, and V. Ramesh, *Shape, Size, and Distribution of Ca(2+) Release Units and Couplons in Skeletal and Cardiac Muscles.* Biophys J, 1999. **77**: p. 1528-39.
12. Franzini-Armstrong, C., *The Relationship between Form and Function Throughout the History of Excitation–Contraction Coupling.* J Gen Physiol, 2018.
13. Asghari, P., D.R. Scriven, S. Sanatani, S.K. Gandhi, A.I. Campbell, and E.D. Moore, *Nonuniform and Variable Arrangements of Ryanodine Receptors within Mammalian Ventricular Couplons.* Circ Res, 2014. **115**: p. 252-62.

14. Asghari, P., M. Schulson, D.R. Scriven, G. Martens, and E.D. Moore, *Axial Tubules of Rat Ventricular Myocytes Form Multiple Junctions with the Sarcoplasmic Reticulum.* Biophys J, 2009. **96**: p. 4651-60.

15. Hayashi, T., M.E. Martone, Z. Yu, A. Thor, M. Doi, M.J. Holst, M.H. Ellisman, and M. Hoshijima, *Three-Dimensional Electron Microscopy Reveals New Details of Membrane Systems for Ca2+ Signaling in the Heart.* J Cell Sci, 2009. **122**: p. 1005-13.

16. Hell, S.W. and J. Wichmann, *Breaking the Diffraction Resolution Limit by Stimulated Emission: Stimulated-Emission-Depletion Fluorescence Microscopy.* Opt Lett, 1994. **19**: p. 780-2.

17. Heilemann, M., S. van de Linde, M. Schuttpelz, R. Kasper, B. Seefeldt, A. Mukherjee, P. Tinnefeld, and M. Sauer, *Subdiffraction-Resolution Fluorescence Imaging with Conventional Fluorescent Probes.* Angew Chem Int Ed Engl, 2008. **47**: p. 6172-6.

18. Baddeley, D., I.D. Jayasinghe, L. Lam, S. Rossberger, M.B. Cannell, and C. Soeller, *Optical Single-Channel Resolution Imaging of the Ryanodine Receptor Distribution in Rat Cardiac Myocytes.* Proc Natl Acad Sci U S A, 2009. **106**: p. 22275-80.

19. Brandenburg, S., J. Pawlowitz, F.E. Fakuade, D. Kownatzki-Danger, T. Kohl, G.Y. Mitronova, M. Scardigli, J. Neef, C. Schmidt, F. Wiedmann*, et al.*, *Axial Tubule Junctions Activate Atrial Ca2+ Release across Species.* Front. Physiol., 2018. **9**.

20. Jayasinghe, I., A.H. Clowsley, R. Lin, T. Lutz, C. Harrison, E. Green, D. Baddeley, L. Di Michele, and C. Soeller, *True Molecular Scale Visualization of Variable Clustering Properties of Ryanodine Receptors.* Cell Reports, 2018. **22**: p. 557-567.

21. Walker, M.A., G.S.B. Williams, T. Kohl, S.E. Lehnart, M.S. Jafri, J.L. Greenstein, W.J. Lederer, and R.L. Winslow, *Superresolution Modeling of Calcium Release in the Heart.* Biophys J, 2014. **107**: p. 3018-3029.

22. Shen, X., J.V.D. Brink, Y. Hou, D. Colli, C. Le, T.R. Kolstad, N. MacQuaide, C.R. Carlson, P.M. Kekenes-Huskey, A.G. Edwards*, et al.*, *3d Dstorm Imaging Reveals Novel Detail of Ryanodine Receptor Localization in Rat Cardiac Myocytes.* J Physiol, 2018.

23. Hou, Y., I. Jayasinghe, D.J. Crossman, D. Baddeley, and C. Soeller, *Nanoscale Analysis of Ryanodine Receptor Clusters in Dyadic Couplings of Rat Cardiac Myocytes.* J Mol Cell Cardiol, 2015. **80**: p. 45-55.

24. Munro, M.L., I.D. Jayasinghe, Q. Wang, A. Quick, W. Wang, D. Baddeley, X.H. Wehrens, and C. Soeller, *Junctophilin-2 in the Nanoscale Organisation and Functional Signalling of Ryanodine Receptor Clusters in Cardiomyocytes.* J Cell Sci, 2016. **129**: p. 4388-4398.

25. Huang, B., W. Wang, M. Bates, and X. Zhuang, *Three-Dimensional Super-Resolution Imaging by Stochastic Optical Reconstruction Microscopy.* Science, 2008. **319**: p. 810-3.

26. Olivier, N., D. Keller, P. Gönczy, and S. Manley, *Resolution Doubling in 3d-Storm Imaging through Improved Buffers.* PLOS ONE, 2013. **8**: p. e69004.

27. Xu, K., G. Zhong, and X. Zhuang, *Actin, Spectrin, and Associated Proteins Form a Periodic Cytoskeletal Structure in Axons.* Science, 2013. **339**: p. 452-6.

28. Yang, T.T., W.M. Chong, W.J. Wang, G. Mazo, B. Tanos, Z. Chen, T.M.N. Tran, Y.D. Chen, R.R. Weng, C.E. Huang*, et al.*, *Super-Resolution Architecture of Mammalian Centriole Distal Appendages Reveals Distinct Blade and Matrix Functional Components.* Nat Commun, 2018. **9**: p. 2023.

29. Bolin, F.P., L.E. Preuss, R.C. Taylor, and R.J. Ference, *Refractive Index of Some Mammalian Tissues Using a Fiber Optic Cladding Method.* Applied Optics, 1989. **28**: p. 2297-2303.

30. Tehrani, K.F., J. Xu, Y. Zhang, P. Shen, and P. Kner, *Adaptive Optics Stochastic Optical Reconstruction Microscopy (Ao-Storm) Using a Genetic Algorithm.* Opt Express, 2015. **23**: p. 13677-92.

31. Schueder, F., J. Lara-Gutierrez, B.J. Beliveau, S.K. Saka, H.M. Sasaki, J.B. Woehrstein, M.T. Strauss, H. Grabmayr, P. Yin, and R. Jungmann, *Multiplexed 3d Super-Resolution Imaging of Whole Cells Using Spinning Disk Confocal Microscopy and DNA-Paint.* Nat Commun, 2017. **8**: p. 2090.

32. Gustavsson, A.K., P.N. Petrov, M.Y. Lee, Y. Shechtman, and W.E. Moerner, *3d Single-Molecule Super-Resolution Microscopy with a Tilted Light Sheet.* Nat Commun, 2018. **9**: p. 123.

33. Chen, F., P.W. Tillberg, and E.S. Boyden, *Optical Imaging. Expansion Microscopy.* Science, 2015. **347**: p. 543-8.

34. Tillberg, P.W., F. Chen, K.D. Piatkevich, Y. Zhao, C.C. Yu, B.P. English, L. Gao, A. Martorell, H.J. Suk, F. Yoshida*, et al.*, *Protein-Retention Expansion Microscopy of Cells and Tissues Labeled Using Standard Fluorescent Proteins and Antibodies.* Nat Biotechnol, 2016. **34**: p. 987-92.

35. Chozinski, T.J., A.R. Halpern, H. Okawa, H.J. Kim, G.J. Tremel, R.O. Wong, and J.C. Vaughan, *Expansion Microscopy with Conventional Antibodies and Fluorescent Proteins.* Nat Methods, 2016. **13**: p. 485-8.

36. Cang, H., Z. Tong, P. Beuzer, Q. Ye, J. Axelrod, and Z. Hong, *Ex-Storm: Expansion Single Molecule Nanoscopy.* bioRxiv, 2016.

37. Gao, M., R. Maraspini, O. Beutel, A. Zehtabian, B. Eickholt, A. Honigmann, and H. Ewers, *Expansion Stimulated Emission Depletion Microscopy (Exsted).* ACS Nano, 2018. **12**: p. 4178-4185.

38. Halpern, A.R., G.C.M. Alas, T.J. Chozinski, A.R. Paredez, and J.C. Vaughan, *Hybrid Structured Illumination Expansion Microscopy Reveals Microbial Cytoskeleton Organization.* ACS Nano, 2017. **11**: p. 12677-12686.

39. Li, R., X. Chen, Z. Lin, Y. Wang, and Y. Sun, *Expansion Enhanced Nanoscopy.* Nanoscale, 2018. **10**: p. 17552-17556.

40. Wang, Y., Z. Yu, C.K. Cahoon, T. Parmely, N. Thomas, J.R. Unruh, B.D. Slaughter, and R.S. Hawley, *Combined Expansion Microscopy with Structured Illumination Microscopy for Analyzing Protein Complexes.* Nature Protocols, 2018. **13**: p. 1869-1895.

41. Cahoon, C.K., Z. Yu, Y. Wang, F. Guo, J.R. Unruh, B.D. Slaughter, and R.S. Hawley, *Superresolution Expansion Microscopy Reveals the Three-Dimensional Organization of the Drosophila Synaptonemal Complex.* Proc Natl Acad Sci U S A, 2017. **114**: p. E6857-e6866.

42. Truckenbrodt, S., M. Maidorn, D. Crzan, H. Wildhagen, S. Kabatas, and S.O. Rizzoli, *X10 Expansion Microscopy Enables 25-Nm Resolution on Conventional Microscopes.* EMBO reports, 2018.

43. Chang, J.B., F. Chen, Y.G. Yoon, E.E. Jung, H. Babcock, J.S. Kang, S. Asano, H.J. Suk, N. Pak, P.W. Tillberg*, et al.*, *Iterative Expansion Microscopy.* Nat Methods, 2017. **14**: p. 593-599.

44. Zhang, Y.S., J.B. Chang, M.M. Alvarez, G. Trujillo-de Santiago, J. Aleman, B. Batzaya, V. Krishnadoss, A.A. Ramanujam, M. Kazemzadeh-Narbat, F. Chen*, et al.*, *Hybrid Microscopy: Enabling Inexpensive High-Performance Imaging through Combined Physical and Optical Magnifications.* Sci Rep, 2016. **6**: p. 22691.

45. Chen, F., A.T. Wassie, A.J. Cote, A. Sinha, S. Alon, S. Asano, E.R. Daugharthy, J.B. Chang, A. Marblestone, G.M. Church*, et al.*, *Nanoscale Imaging of Rna with Expansion Microscopy.* Nat Methods, 2016. **13**: p. 679-84.

46. Zhao, Y., O. Bucur, H. Irshad, F. Chen, A. Weins, A.L. Stancu, E.Y. Oh, M. DiStasio, V. Torous, B. Glass*, et al.*, *Nanoscale Imaging of Clinical Specimens Using Pathology-Optimized Expansion Microscopy.* Nat Biotechnol, 2017. **35**: p. 757-764.

47. Gao, R., S.M. Asano, S. Upadhyayula, I. Pisarev, D.E. Milkie, T.-L. Liu, V. Singh, A. Graves, G.H. Huynh, Y. Zhao*, et al.*, *Cortical Column and Whole Brain Imaging of Neural Circuits with Molecular Contrast and Nanoscale Resolution.* bioRxiv, 2018: p. 374140.

48. Wang, I.E., S.W. Lapan, M.L. Scimone, T.R. Clandinin, and P.W. Reddien, *Hedgehog Signaling Regulates Gene Expression in Planarian Glia.* eLife, 2016. **5**: p. e16996.

49. Mosca, T.J., D.J. Luginbuhl, I.E. Wang, and L. Luo, *Presynaptic Lrp4 Promotes Synapse Number and Function of Excitatory Cns Neurons.* eLife, 2017. **6**: p. e27347.

50. Freifeld, L., I. Odstrcil, D. Forster, A. Ramirez, J.A. Gagnon, O. Randlett, E.K. Costa, S. Asano, O.T. Celiker, R. Gao*, et al.*, *Expansion Microscopy of Zebrafish for Neuroscience and Developmental Biology Studies.* Proc Natl Acad Sci U S A, 2017. **114**: p. E10799-E10808.

51. Jiang, N., H.J. Kim, T.J. Chozinski, J.E. Azpurua, B.A. Eaton, J.C. Vaughan, and J.Z. Parrish, *Superresolution Imaging of Drosophila Tissues Using Expansion Microscopy.* Mol Biol Cell, 2018. **29**: p. 1413-1421.

52. Gambarotto, D., F.U. Zwettler, M. Le Guennec, M. Schmidt-Cernohorska, D. Fortun, S. Borgers, J. Heine, J.-G. Schloetel, M. Reuss, M. Unser*, et al.*, *Imaging Cellular Ultrastructures Using Expansion Microscopy (U-Exm).* Nature Methods, 2019. **16**: p. 71-74.

53. Pesce, L., M. Cozzolino, L. Lanzanò, A. Diaspro, and P. Bianchini, *Enigma at the Nanoscale: Can the Npc Act as an Intrinsic Reporter for Isotropic Expansion Microscopy?* bioRxiv, 2018: p. 449702.

54. Marx, S.O., S. Reiken, Y. Hisamatsu, T. Jayaraman, D. Burkhoff, N. Rosemblit, and A.R. Marks, *Pka Phosphorylation Dissociates Fkbp12.6 from the Calcium Release Channel (Ryanodine Receptor): Defective Regulation in Failing Hearts.* Cell, 2000. **101**: p. 365-76.

55. Tokunaga, M., N. Imamoto, and K. Sakata-Sogawa, *Highly Inclined Thin Illumination Enables Clear Single-Molecule Imaging in Cells.* Nat Methods, 2008. **5**: p. 159-61.

56. Burgoyne, T., E.P. Morris, and P.K. Luther, *Three-Dimensional Structure of Vertebrate Muscle Z-Band: The Small-Square Lattice Z-Band in Rat Cardiac Muscle.* J Mol Biol, 2015. **427**: p. 3527-3537.

57. Wypijewski, K.J., M. Tinti, W. Chen, D. Lamont, M.L.J. Ashford, S.C. Calaghan, and W. Fuller, *Identification of Caveolar Resident Proteins in Ventricular Myocytes Using a Quantitative Proteomic Approach: Dynamic Changes in Caveolar Composition Following Adrenoceptor Activation.* Molecular & Cellular Proteomics, 2015. **14**: p. 596-608.

58. Larcher, V., P. Kunderfranco, M. Vacchiano, P. Carullo, M. Erreni, I. Salamon, F.S. Colombo, E. Lugli, M. Mazzola, A. Anselmo*, et al.*, *An Autofluorescence-Based Method for the Isolation of Highly Purified Ventricular Cardiomyocytes.* Cardiovasc Res, 2018. **114**: p. 409-416.

59. Mortensen, K.I., L.S. Churchman, J.A. Spudich, and H. Flyvbjerg, *Optimized Localization Analysis for Single-Molecule Tracking and Super-Resolution Microscopy.* Nat Methods, 2010. **7**: p. 377-81.

60. Huff, J., *The Airyscan Detector from Zeiss: Confocal Imaging with Improved Signal-to-Noise Ratio and Super-Resolution.* Nature Methods, 2015. **12**: p. 1205.

61. Jayasinghe, I.D., D.J. Crossman, C. Soeller, and M.B. Cannell, *A New Twist in Cardiac Muscle: Dislocated and Helicoid Arrangements of Myofibrillar Z-Disks in Mammalian Ventricular Myocytes.* J Mol Cell Cardiol, 2010. **48**: p. 964-71.

62. Jayasinghe, I., A.H. Clowsley, O. de Langen, S.S. Sali, D.J. Crossman, and C. Soeller, *Shining New Light on the Structural Determinants of Cardiac Couplon Function: Insights from Ten Years of Nanoscale Microscopy.* Front. Physiol., 2018. **9**.

63. Jungmann, R., M.S. Avendano, J.B. Woehrstein, M. Dai, W.M. Shih, and P. Yin, *Multiplexed 3d Cellular Super-Resolution Imaging with DNA-Paint and Exchange-Paint.* Nat Methods, 2014. **11**: p. 313-8.

64. Bovo, E., S. Huke, L.A. Blatter, and A.V. Zima, *The Effect of Pka-Mediated Phosphorylation of Ryanodine Receptor on Sr Ca(2+) Leak in Ventricular Myocytes.* J Mol Cell Cardiol, 2017. **104**: p. 9-16.

65. Huke, S. and D.M. Bers, *Ryanodine Receptor Phosphorylation at Serine 2030, 2808 and 2814 in Rat Cardiomyocytes.* Biochem Biophys Res Commun, 2008. **376**: p. 80-5.

66. Wehrens, X.H., S.E. Lehnart, S. Reiken, J.A. Vest, A. Wronska, and A.R. Marks, *Ryanodine Receptor/Calcium Release Channel Pka Phosphorylation: A Critical Mediator of Heart Failure Progression.* Proc Natl Acad Sci U S A, 2006. **103**: p. 511-8.

67. Wu, Y., H.H. Valdivia, X.H. Wehrens, and M.E. Anderson, *A Single Protein Kinase a or Calmodulin Kinase Ii Site Does Not Control the Cardiac Pacemaker Ca2+ Clock.* Circ Arrhythm Electrophysiol, 2016. **9**: p. e003180.

68. Guo, T., R.L. Cornea, S. Huke, E. Camors, Y. Yang, E. Picht, B.R. Fruen, and D.M. Bers, *Kinetics of Fkbp12.6 Binding to Ryanodine Receptors in Permeabilized Cardiac Myocytes and Effects on Ca Sparks.* Circ Res, 2010. **106**: p. 1743-52.

69. van Oort, R.J., A. Garbino, W. Wang, S.S. Dixit, A.P. Landstrom, N. Gaur, A.C. De Almeida, D.G. Skapura, Y. Rudy, A.R. Burns*, et al.*, *Disrupted Junctional Membrane Complexes and Hyperactive Ryanodine Receptors after Acute Junctophilin Knockdown in Mice.* Circulation, 2011. **123**: p. 979-88.

70. Li, J., M.S. Imtiaz, N.A. Beard, A.F. Dulhunty, R. Thorne, D.F. vanHelden, and D.R. Laver, *Ss-Adrenergic Stimulation Increases Ryr2 Activity Via Intracellular Ca2+ and Mg2+ Regulation.* PLoS One, 2013. **8**: p. e58334.

71. Seyfarth, T., H.P. Gerbershagen, C. Giessler, K. Leineweber, I. Heinroth-Hoffmann, K. Ponicke, and O.E. Brodde, *The Cardiac Beta-Adrenoceptor-G-Protein(S)-Adenylyl Cyclase System in Monocrotaline-Treated Rats.* J Mol Cell Cardiol, 2000. **32**: p. 2315-26.

72. Sun, F., Z. Lu, Y. Zhang, S. Geng, M. Xu, L. Xu, Y. Huang, P. Zhuang, and Y. Zhang, *Stagedependent Changes of B2adrenergic Receptor Signaling in Right Ventricular Remodeling in Monocrotalineinduced Pulmonary Arterial Hypertension.* Int J Mol Med, 2018. **41**: p. 2493-2504.

73. Li, L., J. Li, B.M. Drum, Y. Chen, H. Yin, X. Guo, S.W. Luckey, M.L. Gilbert, G.S. McKnight, J.D. Scott*, et al.*, *Loss of Akap150 Promotes Pathological Remodelling and Heart Failure Propensity by Disrupting Calcium Cycling and Contractile Reserve.* Cardiovasc Res, 2017. **113**: p. 147-159.

74. Kolstad, T.R., J. van den Brink, N. MacQuaide, P.K. Lunde, M. Frisk, J.M. Aronsen, E.S. Norden, A. Cataliotti, I. Sjaastad, O.M. Sejersted*, et al.*, *Ryanodine Receptor Dispersion Disrupts Ca(2+) Release in Failing Cardiac Myocytes.* Elife, 2018. **7**.

75. Pratusevich, V.R. and C.W. Balke, *Factors Shaping the Confocal Image of the Calcium Spark in Cardiac Muscle Cells.* Biophys J, 1996. **71**: p. 2942-57.

76. Scheible, M.B. and P. Tinnefeld, *Quantifying Expansion Microscopy with DNA Origami Expansion Nanorulers.* bioRxiv, 2018: p. 265405.

77. Fowler, E.D., M.J. Drinkhill, R. Norman, E. Pervolaraki, R. Stones, E. Steer, D. Benoist, D.S. Steele, S.C. Calaghan, and E. White, *Beta1-Adrenoceptor Antagonist, Metoprolol Attenuates Cardiac Myocyte Ca(2+) Handling Dysfunction in Rats with Pulmonary Artery Hypertension.* J Mol Cell Cardiol, 2018. **120**: p. 74-83.

78. Fowler, E.D., D. Benoist, M.J. Drinkhill, R. Stones, M. Helmes, R.C.I. Wüst, G.J.M. Stienen, D.S. Steele, and E. White, *Decreased Creatine Kinase Is Linked to Diastolic Dysfunction in Rats with Right Heart Failure Induced by Pulmonary Artery Hypertension.* J Mol Cell Cardiol, 2015. **86**: p. 1-8.

79. Jayasinghe, I.D., M.B. Cannell, and C. Soeller, *Organization of Ryanodine Receptors, Transverse Tubules, and Sodium-Calcium Exchanger in Rat Myocytes.* Biophys J, 2009. **97**: p. 2664-73.

80. Soeller, C., I.D. Jayasinghe, P. Li, A.V. Holden, and M.B. Cannell, *Three-Dimensional High-Resolution Imaging of Cardiac Proteins to Construct Models of Intracellular Ca2+ Signalling in Rat Ventricular Myocytes.* Exp Physiol, 2009. **94**: p. 496-508.

Figures & figure legends

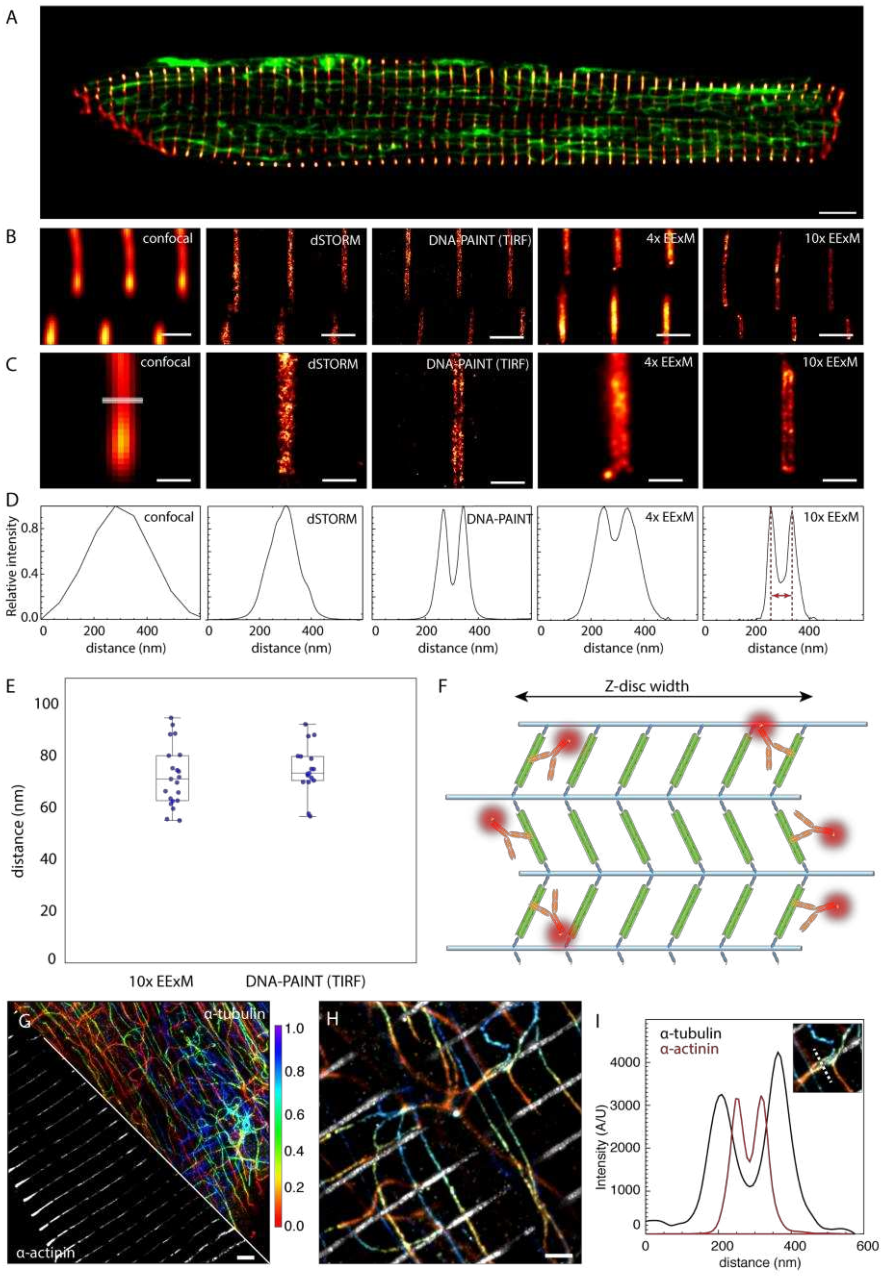

Figure 1. Adaptation of ExM for imaging nanoscale intracellular structures in optically-thick cells. (A) Overview of the shape and size of a rat ventricular myocytes labelled for α-actinin (red hot) and α-tubulin (green). (B) Comparison of z-disc α-actinin immunolabelling in the cell interior mapped with deconvolved confocal microscopy, dSTORM implemented with HiLo illumination, DNA-PAINT implemented in TIRF, 4x EExM (i.e. ExM images acquired with the Airyscan protocol) and 10x EExM. (C) Magnified view of the respective images revealed only DNA-PAINT and 10x EExM could resolve the double-layer morphology of the z-disc reported by the anti-α-actinin Ab. (D) Line profiles taken across the z-discs in the respective images illustrating a bimodal intensity profile with a separation of ~ 70 nm at the peaks in DNA-PAINT, 10x EExM and, to a lesser extent, in 4x EExM data. (E) Dotplots of the measured separation between the α-actinin double-peaks as measured through 10x EExM

and DNA-PAINT (Mean ± SEM: 74.05 ± 3.12 nm and 70.10 ± 2.22 nm respectively; n = 21 and 17; p = 0.31 in two-tailed T-test). Overlaid box and whisker plots illustrate the 5th, 25th, 50th, 75th and 95th percentiles. (F) This double-layer morphology was consistent with a model of the z-disc consisting of six parallel layers of α-actinin (green) anchoring actin filaments (blue); the two outer-most layers are optimally labelled with Abs (orange; see Suppl Fig S2). (G) Maximum intensity projections of a 3D 10x EExM volume of α-actinin (grey) and α-tubulin (coloured for depth, indicated in µm) acquired near the centre of the cell (at a sample depth of ~ 50 µm) illustrate the capability of 10x EExM to image cellular regions far from the surface. (H) Magnified region of the same data illustrates the tessellation between microtubule bundles with the z-discs within ~ 50 nm, illustrated with (I) overlaid intensity profiles of a region (dotted line in inset). Scale bars: A: 5 µm; B, C & H: 1 µm; G: 2 µm. (EExM scale bars adjusted to expansion factor).

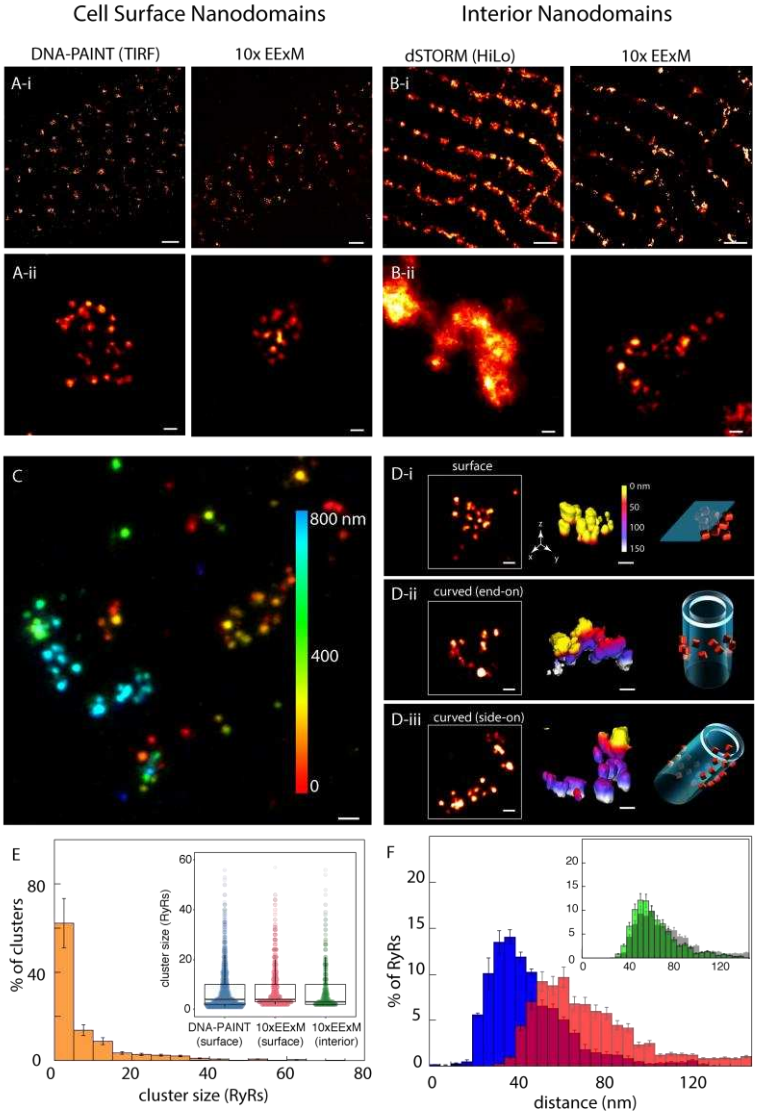

Figure 2. Adaptation of 10x EExM for imaging RyR nanodomain in cardiac muscle cells. (A-i) Comparisons of DNA-PAINT (in TIRF; left) and 10x EExM (right) images of the RyR labelling near the cell surface of rat ventricular cardiac muscle cells, both illustrate domains of RyR labelling whose width is < 500 nm. (A-ii) Magnified views illustrate clearly resolved punctate labelling densities, each corresponding to an individual RyR, in both DNA-PAINT and 10x EExM images. (B-i) Comparisons of dSTORM (with HiLo illumination) and 10x EExM images of RyR nanodomains located in the cell interiors. (B-ii) Magnified views of the respective images illustrate unresolved cluster sub-structure in dSTORM (left) which contrasts with the well-resolved RyR arrays in 10x EExM

in cell interior (right). (C) A depth coded (colour scale in nm) maximum-intensity projection of a 1 µm-deep cell volume with RyR labelling. Comparison of RyR cluster 3D topographies identified with 10x EExM raw data include (D-i) flat RyR arrays at the cell surface and curved nanodomains in cell interior visualised either (D-ii) end-on, along their axis of curvature or (D-iii) side-on, orthogonal to the axis of curvature. Shown, are the in-plane view of the nanodomains (left), surface rendered 3D 10x EExM data, colour coded for depth along the optical axis (z) in nm (middle) and schematic illustration of unique topologies of RyR (orange) arrangement relative to the nearest plasmalemmal membranes (cyan). (E) Percentage histogram of the RyR cluster sizes in the cell interior nanodomains show a Mean ± SEM of 8.23 ± 0.51 RyRs/cluster; n = 11 cells, 1912 clusters. The distributions of the surface cluster sizes, as estimated with both DNA-PAINT (Mean ± SEM of 7.87 ± 0.39 RyRs/cluster; n = 12 cells, 3209 clusters), and the surface and interior clusters imaged 10x EExM, were similar as illustrated by the dot-plots overlaid with the box and whiskers plots (inset; $p > 0.05$ in Bonferroni-adjusted Mann-Whitney tests). (F) The distribution of NND in interior nanodomains with ≥ 5 RyRs (blue) showed a mean of 45.41 ± 0.75 nm. The distribution of 3ND (red) for the same RyR nanodomains had a long rightward tail (mean ± SD: 73.74 ± 14.28 nm). Overlaid with the 3ND histogram of the cell interior (grey, inset), is the equivalent distribution for sub-surface RyR nanodomains (green), which was more left-shifted. Scale bars: A-i & B-i: 1 µm; A-ii & B-ii, C-D: 50 nm. Error bars in plots: SD.

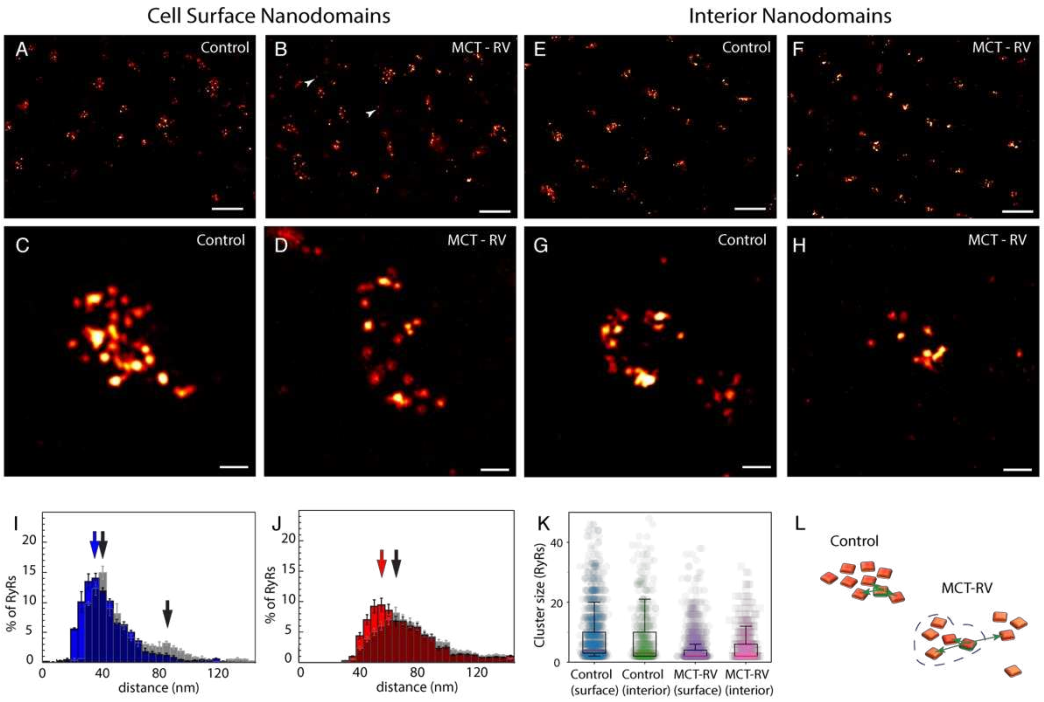

Figure 3. Adaptation of 10x EExM to visualise nanoscale RyR re-arrangement in pathology. Comparison of near-surface RyR organisation in right ventricular cardiomyocytes isolated from (A) control and (B) MCT-RV, which featured noticeably more frequent solitary RyR puncta (arrowheads). Magnified views of (C) control and (D) MCT-RV nanodomains at the cell surface revealed a visibly sparse dispersed RyR arrangement within the nanodomain areas in the latter. RyR nanodomains in the interior of (E) control cells and (F) MCT-RV cells. Magnified view of (G) RyR nanodomains in control cells featured closely clustered RyRs tracing out their curved topography, which contrasted with (H) regions in MCT-RV cell featuring smaller and less discernible nanodomains. (I) NND histogram of Interior nanodomains in MCT-RV cells (grey-shaded) featured a larger mean± SEM (51.65 ± 4.45 nm), a right-shifted primary maximum at ~ 45 nm and a secondary maximum at ~ 85 nm (black arrows) compared to control (blue; mode in blue arrow; mean: 45.41 ± 0.76 nm; $p = 0.001$, df=19 cells; Bonferroni-adjusted Mann-Whitney test). (J) Histograms showing a rightward shift in the mode for the 3NDs for MCT-RV RyRs (grey-shaded; black arrow; mean 91.02 ± 12.88 nm) compared control (red; red arrow; mean: 73.74 ± 14.27 nm; $p=0.0002$, df=19, Bonferroni-adjusted Mann-Whitney test). (K) Dot-plots comparing the cluster size distributions in near-surface and interior nanodomains show a diminished mean and the range of RyR counts in individual clusters in both near-surface ($p<0.0001$; df=20) and interior ($p<0.0001$; df=19) of MCT-RV cells compared to control. (L)

Schematic illustrating how cluster fragmentation in MCT-RV may coincide with the increased NND and 3ND (green arrows) for some RyRs. Scale bars: A,B,E & F: 1 µm and C,D,G &H: 50 nm. Error bars in plots: SD.

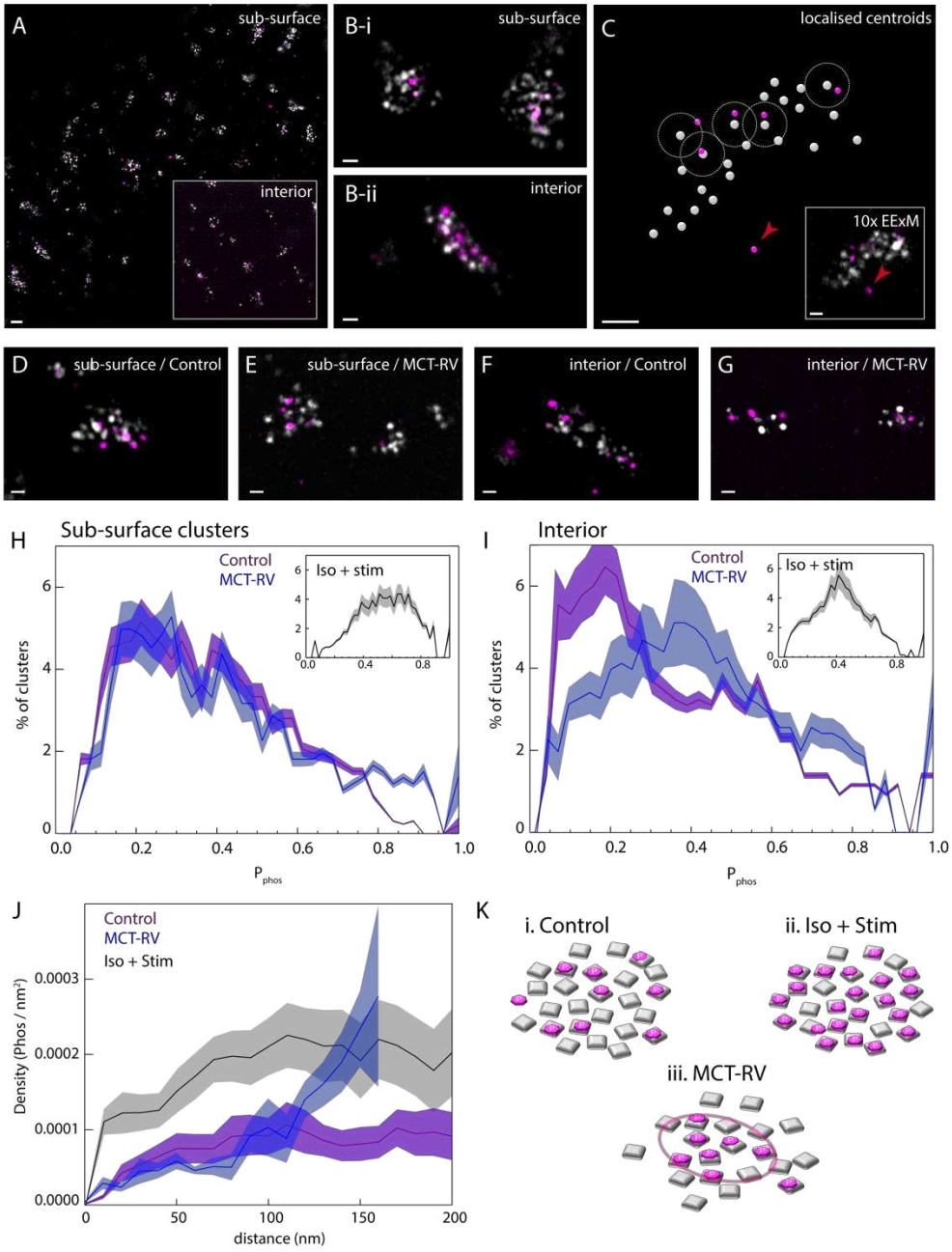

Figure 4. 10x EExM visualisation of variable phosphorylation of RyRs during pathology and acute stimulation. (A) Overlay of 10x EExM images of RyR (grey) and pS2808 (purple) at the surface of a rat ventricular cardiac myocyte. Inset shows the equivalent view in a region ~ 5 µm below the cell surface. (B) Magnified view of nanodomains near (i) the cell surface and (ii) cell interior visually illustrates that punctate pS2808 (purple) labelling densities, observed in fewer numbers, follow either close overlap or proximity with RyR puncta (grey). (C) The centroids of the RyR (grey) and pS2808 puncta (purple) were localised and paired with the nearest RyR within a 30-nm 3D distance (dashed line) to identify RyRs which were phosphorylated at the Ser2808 site. Raw data of region illustrated in inset. An example of unpaired pS2808 marker is shown with an arrowhead. Magnified views of the overlays of sub-surface nanodomains in cells from the right ventricles of (D) control and (E) MCT rats show a minor

fraction of RyRs which associate pS2808 labelling. The same comparison in the cell interior regions illustrate a similar fraction of RyRs with Ser2808 phosphorylation in (F) control nanodomains whilst a greater proportion of RyRs, despite smaller cluster size, coincide with pS2808 labelling in (G) MCT-RV nanodomains. (H) Percentage histograms of the mean fraction of RyRs determined to be phosphorylated at Ser2808 (P_{phos}) in the sub-surface nanodomains containing ≥ 4 RyRs illustrate near-identical distributions (mean ± SD of P_{phos} of 0.31 ± 0.10 and 0.30 ± 0.12; $p > 0.05$; df = 20 cells; Bonferroni-corrected Mann-Whitney t-test) for both control (purple) and MCT-RV (blue). (I) Cell interior nanodomains in MCT-RV (blue; 0.45 ± 0.07) showed a rightward shifted P_{phos} distribution compared to control (purple; 0.27 ± 0.09 ; $p = 0.022$, df = 19). P_{phos} distributions for both sub-surface and interior nanodomains appeared to show a right-shift in control cells stimulated with isoproterenol and simultaneous electrical pacing at 1 Hz (insets). (J) Histograms of the 2D pS2808 localisation density as a function of the distance within the sub-surface nanodomain relative to its boundary in control (purple line), stimulated (black) and MCT-RV (blue) cells. (K-i) In control cells, RyRs phosphorylated at Ser2808 are located, on average, uniformly throughout the nanodomain. (K-ii) Stimulation with isoproterenol and electrical pacing appeared to ~ double the pS2808 density uniformly across the nanodomain. (K-iii) In MCT-RV, a gradient of pS2808 density is seen from the edge of the nanodomain inwards, allowing a sub-domain of potentiated RyRs to be maintained at the centre of the nanodomain (circle). Scale bars: A: 200 nm, B-G: 50 nm

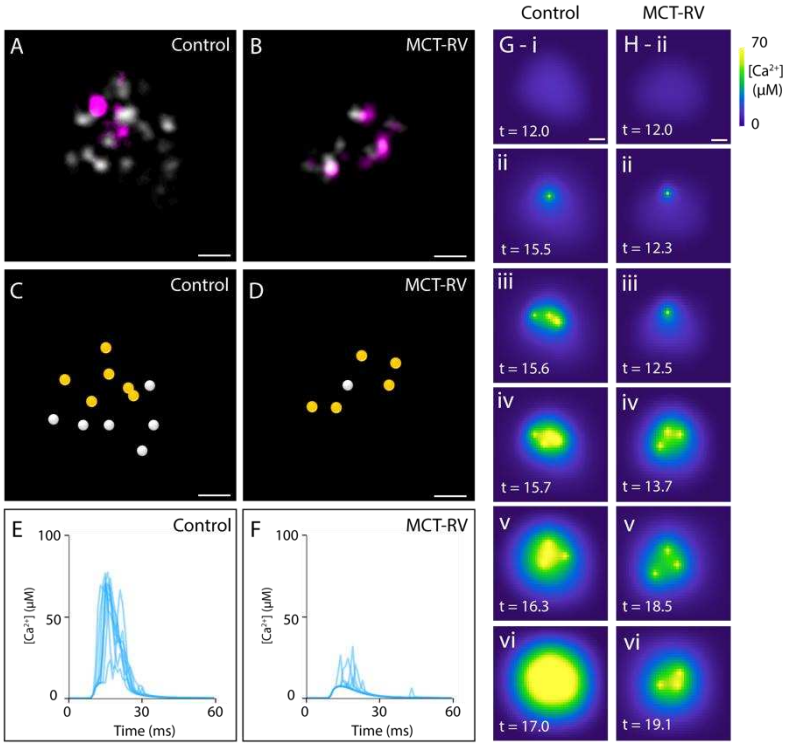

Figure 5. Simulating geometrically-realistic spatiotemporal patterns of Ca^{2+} release based on 10x EExM data. Shown, are examples of RyR (grey) and pS2808 (purple) labelling in approximately median-sized nanodomains of control (A) and MCT-RV cells (B). The centroids of the receptors were localised (circles) and receptors identified as phosphorylated were marked (yellow circles) for the control (C) and MCT-RV (D) clusters. A series of local Ca^{2+} sparks, over-plotted as the time course of the local change in cytoplasmic Ca^{2+} concentration (shown in μM) illustrates how the control (E) geometry facilitates more consistent and pronounced Ca^{2+} release events compared to that in the MCT-RV cluster (F). Spatiotemporal visualisation of the cytoplasmic Ca^{2+} (colour scale shown in μM) at a spatial resolution of 10 nm in the early phases of the Ca^{2+} sparks illustrates progressive recruitment of RyRs, more readily among those phosphorylated at S2808, in the control nanodomain (G) compared to MCT-RV. The latter shows recruitment of RyR openings, however often failed to achieve cluster-wide activation in the first 20 ms of the spark. Scale bars: 50 nm. Time stamps in G&H shown in ms.

For Table of Contents Only